ACS APPLIED MATERIALS & INTERFACES

www.acsami.org

Research Article

Low Lattice Thermal Conductivity in a Wider Temperature Range for Biphasic-Quaternary (Ti,V)CoSb Half-Heusler Alloys

Nagendra S. Chauhan,*,⊥ Dipanwita Bhattacharjee,⊥ Tanmoy Maiti, Yury V. Kolen'ko, Yuzuru Miyazaki, and Amrita Bhattacharya*

Cite This: *ACS Appl. Mater. Interfaces* 2022, 14, 54736−54747

Read Online

ACCESS | Metrics & More | Article Recommendations | Supporting Information

ABSTRACT: Intrinsically high lattice thermal conductivity has remained a major bottleneck for achieving a high thermoelectric figure of merit (zT) in state-of-the-art ternary half-Heusler (HH) alloys. In this work, we report a stable n-type biphasic-quaternary (Ti,V)CoSb HH alloy with a low lattice thermal conductivity $\kappa_L \approx 2$ W m^{-1} K^{-1} within a wide temperature range (300−873 K), which is comparable to the reported nanostructured HH alloys. A solid-state transformation driven by spinodal decomposition upon annealing is observed in $Ti_{0.5}V_{0.5}CoSb$ HH alloy, which remarkably enhances phonon scattering, while electrical properties correlate well with the altering electronic band structure and valence electron count (VEC). A maximum $zT \approx 0.4$ (±0.05) at 873 K was attained by substantial lowering of κ_L and synergistic enhancement of the power factor. We perform first-principles density functional theory calculations to investigate the structure, stability, electronic structure, and transport properties of the synthesized alloy, which rationalize the reduction in the lattice thermal conductivity to the increase in anharmonicity due to the alloying. This study upholds the new possibilities of finding biphasic-quaternary HH compositions with intrinsically reduced κ_L for prospective thermoelectric applications.

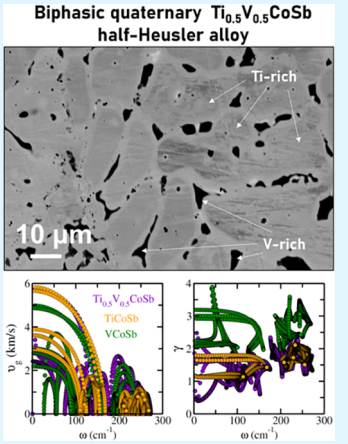

KEYWORDS: *thermoelectrics, spark plasma sintering, transport phenomena, Seebeck coefficient, power factor, microstructure*

1. INTRODUCTION

Half-Heusler (HH) intermetallic phases are cubic structural frameworks that can accommodate varied elemental combinations to exhibit a diverse range of physical properties and phenomena.[1−3] In thermoelectrics (TE), several HH alloys have emerged as a prospective class of cost-effective and high-performance materials for a wide temperature range of applications, owing to their nontoxic and earth-abundant elemental constituents and remarkable power factors.[4−6] First-principles studies on prospective candidates within the HH family indicate an interesting possibility of attaining unique and diverse physical properties.[7−9] Generically, HH alloys being ternary intermetallics, are represented as XYZ, where X, Y, and Z occupy three interpenetrating sublattices to crystallize in a noncentrosymmetric cubic (MgAgAs) $C1_b$ configuration [space group $F\bar{4}3m$ (no. 216)].[10,11] By changing the elemental composition (i.e., X, Y, and Z), the valence electron count (VEC) can be varied to attain electronic behaviors with a wide range of band-gap tunability ranging from semiconducting to superconducting and ferromagnetic to nonmagnetic behaviors.[2,10] However, relatively high thermal conductivity (κ_L), stemming from their simple crystal structure, limits their zT to lower albeit competitive values. Hence, over the past two decades, the key research efforts in HH thermoelectrics have been aimed at the reduction of the thermal conductivity of these materials while maintaining their higher power factor through emerging strategies of alloying-induced phonon engineering,[12−14] nanostructuring,[14−17] defect engineering,[18−21] and nanocompositing approaches.[22−24]

Among the existing HH phases, n-type MNiSn and p-type MCoSb (M = Ti, Zr, Hf) ternary alloys, with ≈18 VEC per unit cell, have been extensively studied and developed for mid−high-temperature TE application.[4,5] Lately, first-principles thermodynamics calculation and experimental realization of new HH materials with 19 VEC, such as VCoSb,[25−29] NbCoSb,[29−31] and TaCoSb,[29] have underpinned the intrinsically defective nature of HH alloys, which has opened a wider possibility in the search of new HH compositions having both higher power factors and inherently lower κ_L. Moreover, stable quaternary compounds based on aliovalent substitution, referred to as double HH alloys, were recently proposed as an alternative to traditional ternary HHs.[32,33] Having smaller group velocity of phonons and enhanced disorder scattering, most of these multicomponent HH derivatives were predicted

Received: September 15, 2022
Accepted: November 16, 2022
Published: November 30, 2022

to exhibit intrinsically lower κ_L, thereby offering a new possibility for the compositional tuning of their transport properties. Notably, the experimental realization of these exotic multinary compositions is, however, challenging owing to materials synthesis limitations. During synthesis, the fusion of elements or simpler compounds into more complex ones is often futile in providing new materials due to the involvement of high energies with limited kinetic control at high temperatures. Mostly, reactions proceed to form the most thermodynamically stable products involving intrinsic phase segregation.[34−39] Interestingly, the high lattice stability of these intrinsically phase-segregated HH alloys provides inherent ability to achieve low κ_L in the synthesized multinary compounds.

In the present study, we report a stable n-type biphasic-quaternary (Ti,V)CoSb HH alloy for high-temperature thermoelectric applications. The material was synthesized using arc melting and consolidated into densified bulk specimens employing spark plasma sintering. The synthesized phase-pure HH alloy crystallizes in a cubic crystal structure and exhibits degenerate n-type semiconducting behavior, which is corroborated using theoretical modeling. Remarkably, the lower $\kappa_L \approx 2$ W m^{-1} K^{-1} within a wide temperature range (300−873 K) was achieved, which is a significantly reduced value when compared to prevailing ternary HH alloys. A maximum $zT \approx 0.4$ ($\pm$0.05) at 873 K is realized, which can be further improved by appropriate doping and panoscopic approaches.[40−43]

2. EXPERIMENTAL DETAILS

The ingots with nominal composition $Ti_{1-x}V_xCoSb$ ($0 < x < 1$) HH alloys were synthesized employing arc melting (AM) under an argon atmosphere using stoichiometric proportions of pure elemental Ti (powder, 99.97%), V (grains, 99.97%), Co (chips, 99.97%), and Sb (shots, 99.98%), purchased from Sigma-Aldrich. The compositional homogeneity was ensured by flipping and remelting AM-ingots three times. After phase composition confirmation, the ingots were ground to a fine powder using a mortar and pestle and then compacted into macroscopic bulk pellets using graphite die employing spark plasma sintering (SPS) by heating up to 1173 K under a uniaxial pressure of 50 MPa in a vacuum of 0.1 mbar. Subsequently, the as-sintered pellets were annealed at 873 K for 4 days. The relative density of a disk-shaped pellet with dimensions of 10 mm × 2 mm was estimated to be ≈99% of the theoretical crystallographic density, as determined by Archimedes principle using an 822*e* analytical balance (Mettler Toledo).

The powder X-ray diffraction (XRD) patterns were collected using a D8 Advance diffractometer (Bruker AXS) equipped with Cu Kα radiation. The XRD patterns were matched to the International Centre for Diffraction Data (ICDD) PDF-4+ database using the X'Pert HighScore software package (PANalytical).[44] The Rietveld refinement was carried out using the Full-Prof software package.[45,46] The phase mapping, morphological features, and compositional homogeneity were investigated in backscattered electron (BSE) mode and secondary electron (SE) mode over the polished sample surfaces using scanning electron microscopy (SEM) coupled to energy-dispersive X-ray (EDX) spectroscopy using a JSM-IT 100 (Jeol) scanning electron microscope.

The temperature-dependent transport measurements were performed on the calibrated instrument following essential considerations to minimize the possibility of erroneous data. The thermal diffusivity (D) was measured using a circular disc specimen of a diameter of 10 mm and thickness of 2 mm, with an LFA467HT HyperFlash laser flash analyzer (Netzsch). Alongside, rectangular bar samples were cut from the circular disk with approximate dimensions of 10 mm × 2 mm × 2 mm for electrical measurements using the ZEM-3 instrument (Ulvac-Riko). The thermal stability and consistency of measured electrical transport properties in synthesized samples were established by overlapping heating and cooling cycles (Figure S1). The carrier concentration (n_H) and mobility (μ_H) were obtained using room-temperature Hall measurements under a magnetic field of 0.5 T. The accuracies in transport measurement were ±6% for thermal diffusivity, ±5% for electrical conductivity, ±5% for Seebeck coefficient, ±10% for specific heat, and ±1% for density.

3. COMPUTATIONAL DETAILS

First-principles DFT calculations[47,48] were performed to obtain the ground-state structure for the synthesized HH compounds. These calculations were performed with a plane wave-based electronic structure theory code, namely, Vienna Ab-initio Simulation Program (VASP).[49,50] The generalized gradient approximation (GGA) as implemented by Perdew−Burke−Ernzerhof (PBE)[51] with projector augmented wave (PAW) potential was used to treat the exchange and correlation, respectively. About 1.3 times the default value in PAW pseudopotential was taken as the cutoff for the plane waves (500 eV). The numerical setting was chosen to yield a convergence energy difference of $<10^{-3}$ eV per atom for structural optimization. The Brillouin zone of the compounds was sampled using a Monkhorst−Pack scheme[52] with converged reciprocal space grids 21 × 21 × 21 per unit cell. The phonon dispersions were calculated using density functional perturbation theory (DFPT), as implemented in the python-based Phonopy code developed by Togo and co-workers.[53] The forces converged to an accuracy of 10^{-8} eV Å^{-1}. The transport coefficients were calculated using Boltz-Trap2,[54] which relies on solving the Boltzmann transport equations under constant relaxation time approximation.

To computationally study the (Ti,V)CoSb HH composition, we generate the most stable ground-state structure of the $Ti_{0.5}V_{0.5}CoSb$ composition using an iterative scanning procedure. For this purpose, we start with the conventional cubic lattice of TiCoSb containing four Ti, four Co, and four Sb atoms. In the first step, we substitute any one of the four Ti atoms with one V atom and relax the structure (since all of the four Ti atoms are symmetrically equivalent); thereby, the ground-state structure of $V_{0.25}Ti_{0.75}CoSb$ is obtained. Using this structure, we iteratively scan the three remaining Ti sites for V substitution to obtain the lowest energy configuration of $Ti_{0.5}V_{0.5}CoSb$. The primitive tetragonal lattice of this lowest energy configuration containing one Ti, one V, two Co, and two Sb atoms is considered for further study (see Figure 1). For $V_{0.25}Ti_{0.75}CoSb$ and $V_{0.75}Ti_{0.25}CoSb$, the conventional cubic lattice is used. To examine the stability of the structure, the formation energy (E_{form}) is computed using

$$E_{form} = E(X_AY_BZ_C) - A\frac{E(X_a)}{a} - B\frac{E(X_b)}{b} - C\frac{E(X_c)}{c} \quad \text{(i)}$$

where $E(X_AY_BZ_C)$ is the total energy of the compound and $E(X_a)$, $E(X_n)$, and $E(X_c)$ are the total energies of the bulk phases of X, Y, and Z having A, B, and C numbers of atoms, respectively. Then, the effect of temperature on formation energy [$E_{form}(T)$] is incorporated by adding the contributions stemming from the vibrational free energy as

$$E_{form}(T) = E_{form} + F_{vib}(T) \quad \text{(ii)}$$

where the free energy contribution is given by $F_{vib}(T)$

https://doi.org/10.1021/acsami.2c16595
ACS Appl. Mater. Interfaces 2022, 14, 54736−54747

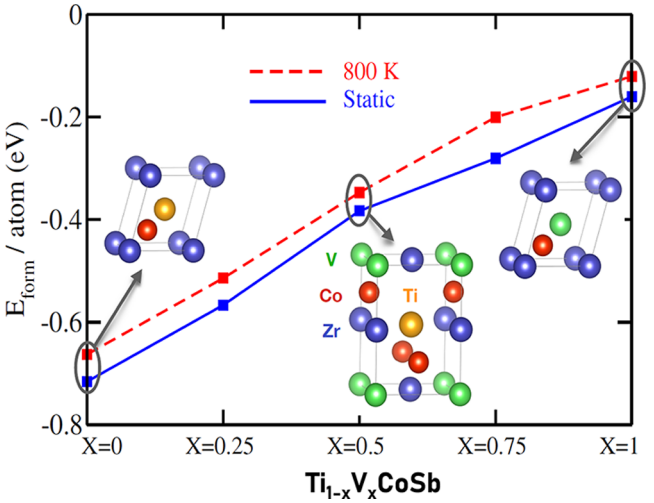

Figure 1. Formation energy per atom (E_{form} atom^{-1}) plotted with the variation in concentration (x) of the X-site element (blue squares) in $Ti_{1-x}V_xCoSb$. The formation energy upon inclusion of the vibration free energy at 800 K is shown in red. The simulation cell for the different compositions is shown in the inset.

$$F_{vib} = F(X_AY_BZ_C) - A\frac{F(X_a)}{a} - B\frac{F(X_b)}{b} - C\frac{F(X_c)}{c} \quad \text{(iii)}$$

Figure 1 shows the formation energy per atom (E_{form} atom^{-1}) plotted for different compositions of $Ti_{1-x}V_xCoSb$ (for X = 0, 0.25, 0.5, 0.75, 1) from their ionic and electronic total energy (static; denoted by blue squares), as well as after including the vibrational free energy contribution at a high temperature of 800 K (red squares). $Ti_{0.5}V_{0.5}CoSb$ (−0.28 eV atom^{-1}) has negative formation energy, which lies between that of TiCoSb (−0.71 eV atom^{-1}) and VCoSb (−0.16 eV atom^{-1}), suggesting its formability and stability. This trend of formation energy is maintained even after including the vibrational contribution.

To compute the relaxation time, a crude strategy as used by previous researchers[55] was adopted. In this approach, the carrier relaxation time (τ) is treated as a constant for a specific temperature and carrier concentration. In a comparison of the theoretical transport coefficients (σ/τ) obtained by solving the semiclassical Boltzmann transport equations as implemented in the BoltzTraP2 package[54] with the experimental values at 800 K and for carrier concentrations of 10^{19} cm^{-3} (TiCoSb), 10^{21} cm^{-3} ($Ti_{0.5}V_{0.5}CoSb$), and 10^{22} cm^{-3} (VCoSb), respectively, we obtain the τ values of 32, 0.154, and 2.2765 fs for TiCoSb, $Ti_{0.5}V_{0.5}CoSb$, and VCoSb, respectively. Thus, we observe a decrease in the order of the $\tau_{e\text{-}ph}$ as we compare TiCoSb to VCoSb and $Ti_{0.5}V_{0.5}CoSb$ to VCoSb.

4. RESULTS

The XRD pattern for the biphasic-quaternary (Ti,V)CoSb HH alloy is shown in Figure 2a for different stages of alloy processing, namely, as-synthesized and annealed arc-melted ingots, as-sintered, and annealed SPS bulk specimens. All of the peaks are well indexed to HH phases and have a cubic crystal system [space group $F\bar{4}3m$ (no. 216)] as shown with hkl indices. Notably, peak splitting of the most intense (220) peaks was observed, as shown by the magnified view in Figure 2b, which indicates the biphasic character of the polycrystals. The Rietveld refinement of the XRD patterns (Figures S2−S5) provides quantitative evaluations of lattice parameters and phase fraction of two phases, which are also tabulated in Table

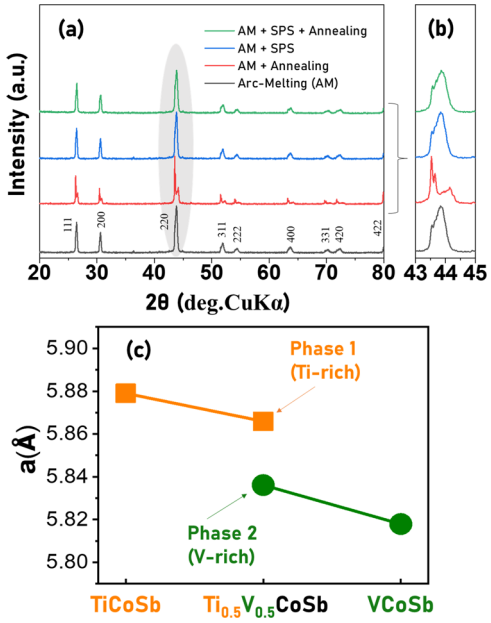

Figure 2. (a) XRD patterns of the as-synthesized and annealed arc-melted ingots along with as-sintered and annealed SPS bulk specimens of $Ti_{0.5}V_{0.5}CoSb$ HH alloy, (b) enlarged view of the XRD patterns in the range of 2θ; = 43−45°, and (c) refined experimental lattice constants indicating contracted and expanded lattice constant of the Ti-rich and V-rich phase in the synthesized biphasic-quaternary $Ti_{0.5}V_{0.5}CoSb$ HH alloy.

1. The lattice parameter (a) obtained for the Ti-rich phase and V-rich phase in arc-melted (Ti,V)CoSb HH alloy indicates the respective solubility of V and Ti within the biphasic-quaternary HH alloy, while cation size difference ($r_{Ti} > r_V$) is found to decrease and increase the cubic lattice constant a for the Ti-rich HH phase and V-rich HH phase, owing to the solubility of V and Ti in their partially substituted (Ti,V) sublattice. During the sintering of the arc-melted ingots, no discernible change was recognized for the peak position and shape, and the lattice parameter varies marginally. The pronounced low-angle shoulder observed for the as-synthesized arc-melted ingots and the as-sintered SPS bulk specimens indicates a greater phase fraction of the V-rich phase, as shown in Table 1.

Upon annealing of the arc-melt ingot, the peaks get separated into lower-angle sharper peaks and higher-angle shoulders, implying the increased phase fraction for the Ti-rich HH phase. The V-rich HH phase that predominates in the arc-melted ingots and sintered SPS bulk specimens is found to be reduced upon annealing. Interestingly, the changes in the lattice parameters upon annealing (Table 1) for the phases indicate immiscibility driven by spinodal decomposition of the VCoSb−TiCoSb HH phase system. The annealed SPS bulk samples were found to be thermally stable and exhibit equivalent phase fractions for both phases. However, compared to the annealing of arc-melted ingot, relatively higher solubility of V and Ti in Ti-rich HH phases and V-rich HH phases was found for prolonged annealing of SPS bulk specimens. The altered phase fractions for different heat treatments imply the metastable nature of the synthesized quaternary (Ti,V)CoSb HH alloy, which upon annealing undergoes phase segregation to reach thermal stability.

The calculated lattice parameters of the annealed (Ti,V)-CoSb HH alloy are shown in Figure 2c. The equilibrium lattice constant for the conventional lattice of TiCoSb is found to be

https://doi.org/10.1021/acsami.2c16595
ACS Appl. Mater. Interfaces 2022, 14, 54736−54747

Table 1. Rietveld Refined Parameters of Biphasic-Quaternary $Ti_{0.5}V_{0.5}CoSb$ Half-Heusler Alloy[a]

	phase 1 (Ti-rich)			phase 2 (V-rich)		
	a (Å)	phase (%)	density	a (Å)	phase (%)	density
AM	5.8702(1)	42.9	7.50	5.8420(1)	57.9	7.71
AM + annealing	5.8819(1)	55.3	7.46	5.8205(1)	44.7	7.80
AM + SPS	5.8710(1)	37.9	7.50	5.8413(1)	62.1	7.71
AM + SPS + annealing	5.8659(1)	49.4	7.52	5.8361(1)	50.6	7.74

[a]AM = arc melting and SPS = spark plasma sintering.

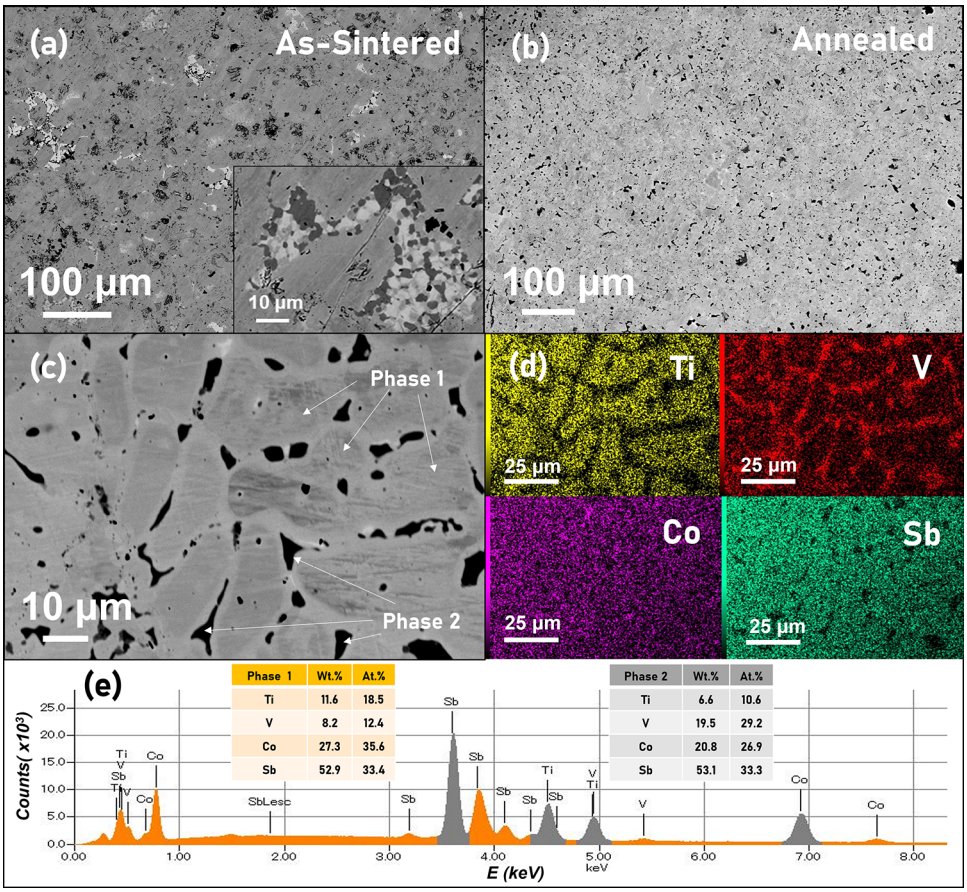

Figure 3. BSE−SEM images at low magnification showing the (a) as-sintered microstructure with biphasic regions shown in the inset and (b) annealed microstructure with a well-distributed and phase-separated biphasic microstructure. (c) High-magnification image indicating phase separation, and (d) respective SEM−EDX elemental maps indicating bright Ti-rich region 1 and dark V-rich region 2. (e) EDX spectrum and quantitative composition tabulated in the inset for the synthesized biphasic-quaternary $Ti_{0.5}V_{0.5}CoSb$ HH alloy.

higher (≈5.89 Å) than that of VCoSb (≈5.82 Å), which can be mainly attributed to the cation radius size difference ($r_V < r_{Ti}$). Interestingly, partial substitution at the (Ti,V) sublattice is evident by decreasing and increasing lattice constant in TiCoSb and VCoSb HH phases, respectively. These observations suggest the biphasic nature of (Ti,V)CoSb HH with intermediate VEC composition, wherein a spinodal decomposition-driven biphasic microstructure exists with TiCoSb and VCoSb phases having a partially substituted (Ti,V) sublattice, which is schematically displayed in the inset of Figure 1. The theoretical formation energy (E_{form} atom^{-1}) calculations (Figure 1) indicate that the nominal $Ti_{0.5}V_{0.5}CoSb$ HH phase has intermediate formation energy (−0.28 eV atom^{-1}) as compared to both its pristine constituting counterparts [TiCoSb (−0.71 eV atom^{-1}) and VCoSb (−0.16 eV atom^{-1})]. The occurrence of spinodal decomposition promoting phase segregation with equiatomic phase fractions of Ti-rich and V-rich HH phases within the annealed sintered bulk specimens is also observed.

The microstructural characterization of the synthesized (Ti,V)CoSb HH alloy is shown in Figure 3. A densely packed microstructure is evidenced by a low magnification BSE−SEM image for the as-sintered and annealed SPS samples (Figure 3a,b). The as-sintered samples exhibit heterogeneously distributed regions with biphasic structures appearing in localized areas, as shown in the inset of Figure 3a. During annealing, the distribution appears more homogeneous as indicated by Figure 3b. The equiaxed microstructure, shown in Figure 3c at high magnification, reveals two compositionally distinct and phase-segregated types of phases, which correspond to V-rich (dark regions) and Ti-rich (gray regions) phases, as indicated within the annealed (Ti,V)CoSb HH alloy. Alongside their energy-dispersive X-ray (EDX) spectroscopy, elemental mappings (Figure 3d) confirm that the two phases

https://doi.org/10.1021/acsami.2c16595
ACS Appl. Mater. Interfaces 2022, 14, 54736−54747

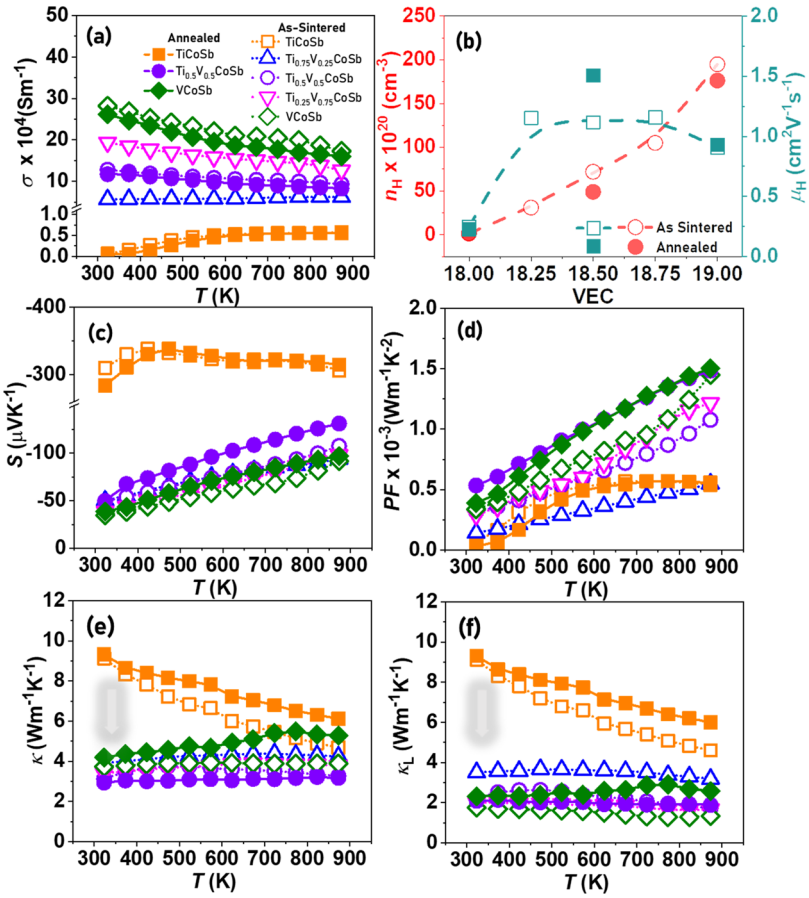

Figure 4. Thermoelectric transport properties of the synthesized $Ti_{1-x}V_xCoSb$ ($0 < x < 1$) half-Heusler alloys: (a) electrical conductivity (σ), (b) carrier concentration (n_H) and carrier mobility (μ_H) as a function of valence electron count (VEC) per unit cell, (c) Seebeck coefficient (S), (d) power factor (PF), (e) total thermal conductivity (κ), and (f) lattice thermal conductivity (κ_L).

Table 2. Hall Measurement of Synthesized $Ti_{1-x}V_xCoSb$ ($0 < x < 1$) Half-Heusler Samples at Room Temperature[a]

compositions		R_H ($m^3\ C^{-1}$) × 10^{-9}	n_H (cm^{-3}) × 10^{20}	μ_H($cm^2\ V^{-1}\ s^{-1}$)	m^*/m_e
AM + SPS	TiCoSb	−62.4(1)	1.0	0.25	
	$Ti_{0.75}V_{0.25}CoSb$	−2.05(1)	30.5	1.15	5.22
	$Ti_{0.5}V_{0.5}CoSb$	−0.873(1)	71.5	1.12	9.14
	$Ti_{0.25}V_{0.75}CoSb$	−0.597(2)	104.5	1.16	9.15
	VCoSb	−0.321(2)	194.4	0.90	12.4
Annealed	TiCoSb	−80.4(1)	0.78	0.22	
	$Ti_{0.5}V_{0.5}CoSb$	−1.29(2)	48.5	1.51	9.61
	VCoSb	−0.355(2)	176	0.93	12.9

[a]AM = arc melting and SPS = spark plasma sintering.

existing as V-rich and Ti-rich phases with a partially substituted (Ti, V) sublattice having varying stoichiometry. The variation in the stoichiometry in these two regions was examined using EDX, and the recorded spectrum is shown in Figure 3e and quantitatively tabulated for both Ti-rich HH (Phase 1) and V-rich HH (Phase 1) phases in the inset. The obtained results quantitatively confirm the biphasic-quaternary nature driven by spinodal decomposition of the VCoSb−TiCoSb HH phase system having a partially substituted (Ti,V) sublattice, thereby demonstrating the critical role of heat treatment in solid-state phase transformation.

For comparison, the measured transport properties of as-sintered (open symbols) and annealed (filled symbols) samples of $Ti_{1-x}V_xCoSb$ ($0 < x < 1$) HH alloys are presented. The temperature-dependent electrical conductivity (σ), shown in Figure 4a, indicates a degenerate semiconducting behavior (i.e., σ decreases with increasing temperature) for $x > 0.25$, while TiCoSb demonstrates a typical semiconducting behavior (i.e., σ increases with increasing temperature). A lower σ was measured for VCoSb, TiCoSb, and $Ti_{0.5}V_{0.5}CoSb$ upon annealing, which can be attributed to structural ordering in TiCoSb HH,[6,56] enhanced V-vacancy defect for VCoSb,[26] and occurrence of spinodal decomposition in the synthesized biphasic-quaternary $Ti_{0.5}V_{0.5}CoSb$ HH alloy.

The temperature-dependent σ values in the measured temperature range show a direct correlation to VEC. To reveal carrier characteristics, the results of Hall measurements conducted at room temperature are shown in Figure 4b and Table 2. For as-sintered $Ti_{1-x}V_xCoSb$ ($0 < x < 1$) HH alloys, higher VEC corresponds to higher carrier concentrations (n_H)

https://doi.org/10.1021/acsami.2c16595
ACS Appl. Mater. Interfaces 2022, 14, 54736−54747

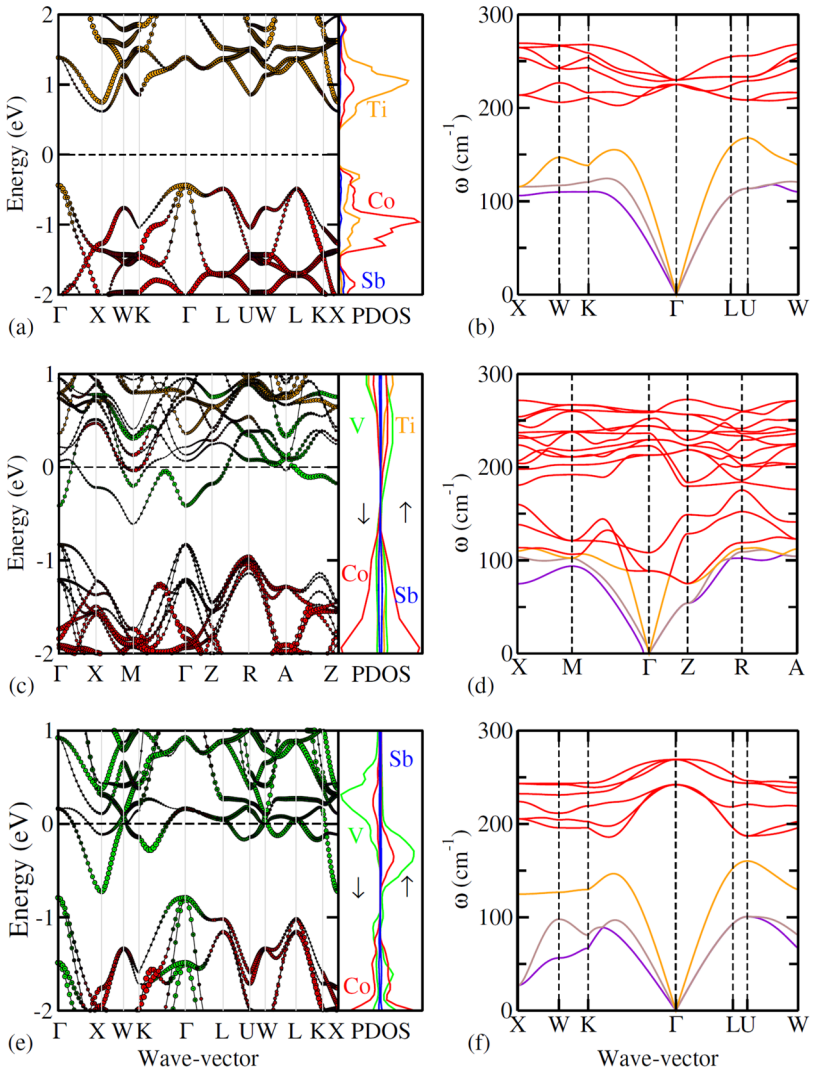

Figure 5. Electronic band structure shown alongside with spin-resolved density of states (a, c, e) and phonon dispersion curves (b, d, f) for TiCoSb (a, b), (Ti,V)CoSb (c, d), and VCoSb (e, f) half-Heusler alloys.

with a significant difference in the order of TiCoSb (10^{19} cm^{-3}) > (Ti, V)CoSb (10^{21} cm^{-3}) > VCoSb (10^{22} cm^{-3}). As reported previously,[26,27] the synthesized VCoSb HH alloy also exhibits a relatively high μ_H that has been related to the metallic characteristics arising from the presence of one electron in the conduction band. TiCoSb HH alloys show relatively lower n_H and μ_H, explaining their semiconducting properties and lower σ, consistent with previous reports on TiCoSb HH alloys.[56−58] Although a linear increase in n_H with increasing VEC was observed for intermediate $Ti_{1-x}V_xCoSb$ HH alloys ($0.25 < x < 0.75$), a marginal change in μ_H was observed, which is comparable to VCoSb HH, implying stronger carrier scattering at higher n_H. Upon annealing, a higher μ_H but reduced n_H was measured for VCoSb, TiCoSb, and $Ti_{0.5}V_{0.5}CoSb$ (Table 2), which correlates with the lowering σ upon annealing.

Figure 4c displays the temperature-dependent Seebeck coefficient (S) exhibiting negative values that indicate n-type conduction with electrons as majority charge carriers. As reported previously,[56−58] TiCoSb HH alloy demonstrates a remarkably high $S \approx 300\ \mu V\ K^{-1}$ in the measured temperature range, while VCoSb HH alloy displays a relatively low S. For the as-sintered intermediate $Ti_{1-x}V_xCoSb$ HH alloys ($0.25 < x < 0.75$), S values are closely related to VCoSb and can be attributed to their high n_H. S holds an inverse relationship with σ and increases with increasing temperature. To understand the degenerate electrical transport of the synthesized $Ti_{1-x}V_xCoSb$ HH alloys ($0.25 < x < 1$), we estimated the carrier effective mass (m^*) based on energy-independent relaxation time approximation, assuming a single parabolic band using the Pisarenko relationship between S and n, which is expressed as $S = (8\pi^2k_B^2/3eh^2)m^*T(\pi/3n)^{2/3}$, wherein k_B and h are the Boltzmann constant and Planck's constant, respectively.[59,60] The evaluated m^* (Table 2) follows TiCoSb < (Ti, V)CoSb < VCoSb, where m_e represents the mass of an electron, suggesting an increased effective mass with the VEC increase of the HH composition. A higher S was measured for annealed $Ti_{0.5}V_{0.5}CoSb$ HH alloys, which can be ascribed to reduced n_H and increased m^* upon annealing due to the occurrence of spinodal decomposition. The higher m^* explains the low μ_H measured for these synthesized HH alloys. Figure 4d shows the trend of the power factor (PF, $S^2\sigma$), which increases with increasing temperature, displaying a high value for $Ti_{0.5}V_{0.5}CoSb$ HH in the measured temperature range, reaching $\approx 1.6 \times 10^{-3}$ W m^{-1} K^{-2} at 700 K. The electrical transport properties of annealed biphasic-quaternary

https://doi.org/10.1021/acsami.2c16595
ACS Appl. Mater. Interfaces 2022, 14, 54736−54747

$Ti_{0.5}V_{0.5}CoSb$ HH alloy exhibit high thermal stability and are retained even under cycling conditions (Figure S1).

The total thermal conductivity κ was evaluated using the equation $\kappa = D \times \rho \times C_p$ (Figure 4e). Interestingly, κ is significantly lower and varies marginally in the measured temperature range, which can be ascribed to the defect chemistry and alloy scattering supplemented by mass and strain fluctuation, all of which synergistically enhance phonon scattering. The measured values for pristine VCoSb[25−28] and TiCoSb[56−58] HH alloys are comparable to previous reports. Upon annealing, the occurrence of spinodal decompositions further lowers the κ significantly for a wide temperature range, which is comparable to the κ obtained in bulk nanostructured ternary HH alloys. The electronic thermal conductivity was experimentally estimated according to Wiedemann−Franz law $\kappa_e = L \times \sigma \times T$, where L is the Seebeck-dependent Lorenz number.[61] The L values and κ_e are shown in Figure S6. The κ_e for the synthesized $Ti_{1-x}V_xCoSb$ HH alloys ($0.25 < x < 1$) has a significant contribution to κ because of higher σ, which increases with increasing temperature. The κ_L (Figure 4e) is calculated using the equation $\kappa_L = \kappa - \kappa_e$ along with κ. The κ_L of the synthesized $Ti_{1-x}V_xCoSb$ HH alloys ($0.25 < x < 0.75$) is found to be significantly suppressed in comparison to TiCoSb HH alloys, especially at a lower temperature. Interestingly, while κ_L for VCoSb is increased upon annealing, the annealed $Ti_{0.5}V_{0.5}CoSb$ HH alloys display a further lowering in κ_L over a wide temperature range. This can be ascribed to the occurrence of spinodal decomposition. The unusual lowering in κ_L for VCoSb, which increases with increasing temperature below 800 K, can be associated with the presence of inherent vacancies and V/Co disordering,[29] experimentally yielding unexpectedly low κ values as compared to theoretical estimates reported previously.[25−28]

5. DISCUSSION

5.1. Critical Role of VEC on Electrical Transport. In HH alloys, VEC plays a predominant role in determining the intrinsic transport properties, and its variation provides an inherent ability to modify both the electronic band structure and microstructure simultaneously. To understand the implications of the variation of VEC in $Ti_{1-x}V_xCoSb$ HH alloys ($0.25 < x < 1$), the electronic density of states (DOS) and band structure of TiCoSb, $Ti_{0.5}V_{0.5}CoSb$, and VCoSb HH alloys are compared (Figure 5a,c,e). The band gap between valence and conduction bands arises from the strong hybridization of d-states of the V, Ti, and Co transition metal atoms. TiCoSb exhibits a larger band gap $E_g \approx 1.046$ eV, consistent with previous calculations.[62,63] The VEC variation by equiatomic Ti substitution with V in $Ti_{0.5}V_{0.5}CoSb$ HH alloys shifts the E_F into the conduction band, thereby leading to almost metallic DOS near the E_F.

In TiCoSb, VCoSb, and $Ti_{0.5}V_{0.5}CoSb$ HH alloys, V and Ti contribute mostly to the conduction band, i.e., to states lying above the gap, while Co contributes majorly to the valence band, i.e., to states lying below the energy gap. The contribution of p-states of Sb in most HH alloys is largely limited to core states with minimal contribution to DOS near E_F. A sharp d-state peak is observed within the conduction band in pristine ternary TiCoSb and VCoSb HH alloys, which is flattened in biphasic-quaternary (Ti,V)CoSb HH alloy. Thus, a partially substituted (Ti,V) sublattice in $Ti_{1-x}V_xCoSb$ HH alloys ($0.25 < x < 1$) can be regarded as an intermediate VEC. Nominal $Ti_{0.5}V_{0.5}CoSb$ exhibits an intermediate VEC that significantly modifies the Fermi surface shape and related transport properties, such as electron group velocities, lifetimes, and effective masses of electrons, which resembles VCoSb HH electronic DOS and explains the observed electrical transport trends.

Interestingly, $Ti_{0.5}V_{0.5}CoSb$ HH alloy exhibits spin polarization as seen from the spin-resolved DOS, which arises from the magnetic nature of VCoSb. In VCoSb, the E_F is located well within the conduction band with more pronounced changes observed in spin-resolved DOS, suggesting it to be highly magnetic (Figure S7). One of the spin channels has a finite band gap of 0.86 eV (contributed by V and Co d-states at the CBM and VBM), whereas the other has a very small band gap of ≈0.3 eV (V and Co d-states at the CBM and VBM, respectively). Similar to it, $Ti_{0.5}V_{0.5}CoSb$ has a finite band gap of 0.75 eV (Figure S5b) for the majority spin and a smaller band gap of ≈0.2 eV for the minority spin.

5.2. κ_L Reduction Comparable to Nanostructured Alloys over a Wider Temperature Range. Alloying induces mass and strain fluctuations within the microstructure for point defect scattering of phonons with a shorter mean free path (MFP). Such scattering is prevalent at higher temperatures and can be augmented by introducing interstitial atoms and/or vacancies in a crystal. For lower-temperature regimes, nanostructuring-induced grain boundary scattering is most effective and targets the phonons with medium MFP. In the synthesized (Ti,V)CoSb HH alloy, a significant reduction in κ_L was observed over a wider temperature range, corresponding to ≈60 and ≈30% reduction compared to its pristine TiCoSb and VCoSb counterparts, respectively. This can be mainly ascribed to the biphasic nature of (Ti,V)CoSb HH alloy, which comprises mass contrast and local bond strain induced by the defects, phase segregation stimulated mesoscale grain boundaries. Such phonon scattering is comparable to bulk nanostructuring and can be further enhanced by panoscopic approaches.[40−43]

The implication of the biphasic-quaternary nature of (Ti,V)CoSb HH alloy on the thermal transport scenario is elucidated in Figure 5b,d,f. The acoustic modes of the phonon dispersion spectrum, which generally contribute to 90% of the heat transport,[64,65] are highlighted in purple, brown, and orange in Figure 5, representing TA, TA′, and LA modes, respectively. In both TiCoSb and VCoSb, the highest frequency of the acoustic modes extends up to ≈150 cm^{-1}. However, for $Ti_{0.5}V_{0.5}CoSb$, the acoustic modes are suppressed to ≈115 cm^{-1}, which is indicative of a lowering in κ_L, since the highest acoustic frequency is related to the Debye temperature of the lattice that directly dictates the κ_L.[64,65] However, the group velocity of the TA and TA′ modes for $Ti_{0.5}V_{0.5}CoSb$ is found to be comparable to that of VCoSb, whereas that of the LA mode is similar to TiCoSb (Figure 6a), suggesting the moderate value of κ_L (group velocity being directly dependent on κ_L) as compared to pristine ones.[66] Similarly, κ_L also depends on the degree of anharmonicity in the lattice, which is related to the Grüneisen parameter (γ).[4,26,67] γ for the pristine compositions and $Ti_{0.5}V_{0.5}CoSb$ is plotted as a function of frequency in Figure 6b. γ of VCoSb is found to be the highest, implying very high anharmonicity, while it is found to be the lowest for TiCoSb for all frequencies. γ for $Ti_{0.5}V_{0.5}CoSb$ is found to be transitional, implying moderate anharmonicity and, hence, an intermediate value of κ_L as compared to the pristine ones.

https://doi.org/10.1021/acsami.2c16595
ACS Appl. Mater. Interfaces 2022, 14, 54736−54747

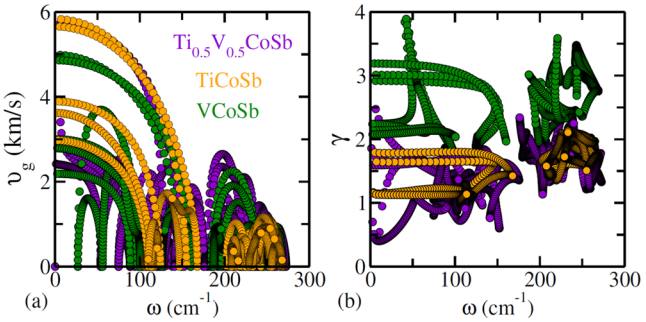

Figure 6. Comparison of group velocity (a) and Grüneisen parameter (b) for TiCoSb (orange), VCoSb (green), and $Ti_{0.5}V_{0.5}CoSb$ (indigo) half-Heusler alloys.

The theoretical calculation of the phonon spectrum is based on the $Ti_{0.5}V_{0.5}CoSb$ alloy, instead of biphasic-quaternary (Ti,V)CoSb. Thus, to explain the low κ_L in biphasic-quaternary (Ti,V)CoSb, the disorder scattering parameter (Γ) is also evaluated and shown in Table 3, while the calculation details

Table 3. Calculated Disorder Parameter (Γ) and the Scattering Parameters due to Mass (Γ_m) and Strain Field Fluctuations (Γ_s) of Synthesized $Ti_{1-x}V_xCoSb$ ($0 < x < 1$)

compositions	Γ	Γ_m	Γ_s	ε	γ	υ_P
TiCoSb					1.56	0.262
$Ti_{0.75}V_{0.25}CoSb$	0.014	0.00016	0.022	103	1.61	0.352
$Ti_{0.5}V_{0.5}CoSb$	0.019	0.0002	0.050	169	1.67	0.442
$Ti_{0.25}V_{0.25}CoSb$	0.015	0.00015	0.067	289	1.72	0.531
VCoSb	0.19	0.04600	0.144	528	1.78	0.621

are discussed in Section S1. For intermediate $Ti_{1-x}V_xCoSb$ HH alloys ($0.25 < x < 0.75$), the phenomenological adjustable parameter (ε), and Poisson ratio (υ_P) were evaluated based on previous reports on the elastic properties of VCoSb and TiCoSb.[4,26] As shown in Table 3, the Γ for nominal VCoSb owing to vacancy concentration is an order higher than other intermediate compositions, indicating significant phonon scattering and explaining the lowest κ_L observed for as-synthesized VCoSb HH alloys. However, for annealed VCoSb, the κ_L increases in magnitude and with temperature, which can be ascribed to increasing V-deficiency in VCoSb HH alloy as observed previously, wherein with increasing V-deficiency in VCoSb, higher κ_L was measured.[28] Also, the higher κ_L for annealed TiCoSb HH corroborates well with the previous report on the annealing effect in TiCoSb HH alloy, which suggests that changes of TE transport properties upon annealing are driven by two competitive phenomena: the structural disorder is induced due to evaporation of impurity antimony while the structural ordering is promoted by annealing.[56]

Interestingly, the structural ordering of the transitional $Ti_{1-x}V_xCoSb$ HH alloy ($0.25 < x < 0.75$) compositions promotes spinodal decomposition, which enhances phonon scattering, resulting in lower κ_L upon annealing. Thus, although the theoretical calculations show moderate γ for $Ti_{0.5}V_{0.5}CoSb$ as compared to defective VCoSb, upon annealing, the scattering of phonons in all MFPs ranging from nano- to microlength scales can be achieved in such biphasic-quaternary alloys, which synergistically integrates solid solution point defects, nanostructures, and grain boundary interfaces within the microstructure. Thus, for annealed samples, the biphasic-quaternary HH alloys have a greater potential to significantly reduce κ_L to the minimum theoretical limit than the defective VCoSb HH alloy.

5.3. Enhanced n-Type Thermoelectric Performance in CoSb-Based HH Alloys. Cobalt antimonide-based ternary HH alloys, e.g., MCoSb (VEC ≈ 18) and VCoSb (VEC ≈ 19), exhibit remarkable electrical transport. As prospective TE material, TiCoSb has attracted considerable interest owing to its high thermopower (≈300 μV K^{-1}) in a wider temperature range, while VCoSb surprisingly demonstrates degenerate semiconducting behavior despite having VEC ≈ 19. The implication of such behavior of transport properties is also corroborated by theoretical studies (Figure 7) evaluated to 800

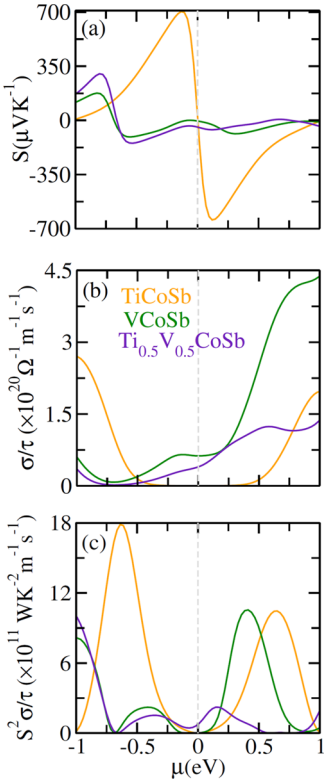

Figure 7. Transport properties of TiCoSb (orange), VCoSb (green), and $Ti_{0.5}V_{0.5}CoSb$ (indigo) half-Heusler alloys at 800 K: (a) Seebeck coefficient (S), (b) electrical conductivity (σ/τ), and (c) power factor ($S^2\sigma/\tau$) plotted as a function of electronic chemical potential (μ).

K. The Seebeck coefficient for TiCoSb (VEC ∼ 18) is significantly higher than that of VCoSb (VEC ∼ 19) as displayed in Figure 7a, whereas the electrical conductivity (scaled by relaxation time) shown in Figure 7b is much higher for VCoSb and $Ti_{0.5}V_{0.5}CoSb$ as compared to TiCoSb due to the presence of a higher electron count (leading to inherent doping characteristics). Thus, the improvement of the power factor (scaled by relaxation time) for the substituted compound ($Ti_{0.5}V_{0.5}CoSb$) is restricted, and this can be seen in Figure 7c. Interestingly, both pristine ternary TiCoSb and VCoSb exhibit n-type conduction with an indirect band gap arising from the hybridization between d-states from the constituting transition metals (as seen from the band structure plots). However, the best p-type thermoelectric properties for HH thermoelectrics in the midtemperature range were achieved in the optimally substituted MCoSb alloys.

https://doi.org/10.1021/acsami.2c16595
ACS Appl. Mater. Interfaces 2022, 14, 54736−54747

From an application perspective, the TE performance of n-type MCoSb-based HH alloys has so far remained insignificantly low and needs further improvement to make them compatible with their high-performance p-type counterpart. In HH thermoelectrics, CoSb-based alloys are mostly considered for p-type TE properties. The as-sintered and annealed samples of $Ti_{1-x}V_xCoSb$ ($0 < x < 1$) HH alloys are shown in Figure 8a,

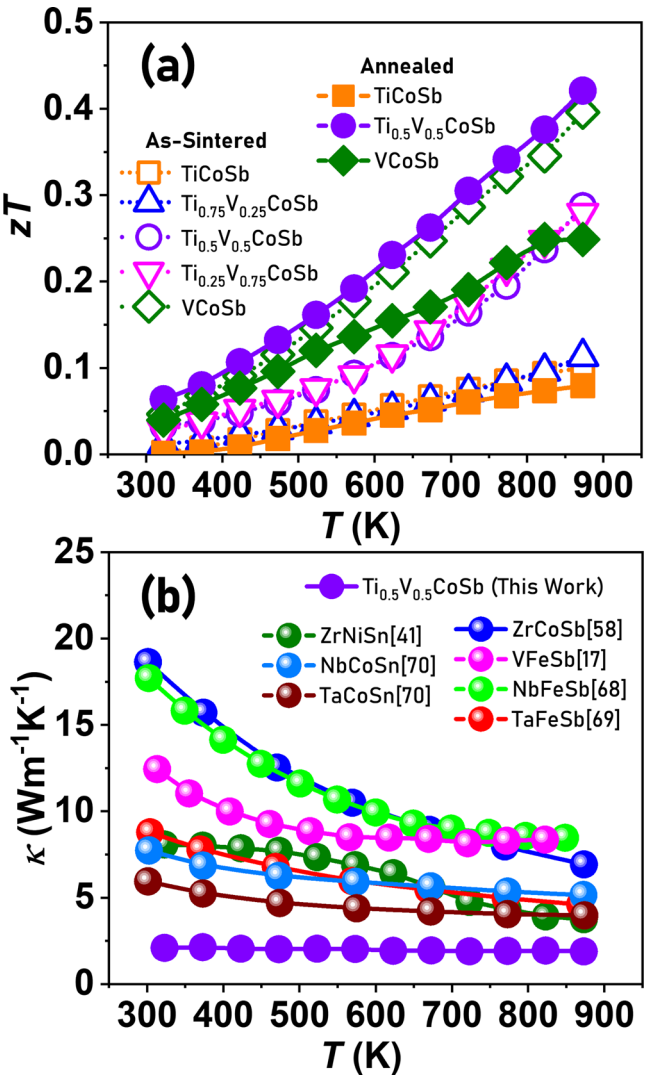

Figure 8. (a) Temperature-dependent zT for the as-sintered and annealed bulk specimens of $Ti_{1-x}V_xCoSb$ ($0 < x < 1$) half-Heusler alloys. (b) Comparison of the synthesized biphasic-quaternary $Ti_{0.5}V_{0.5}CoSb$ HH alloy with VEC ~ 18 half-Heusler alloys.

demonstrating the critical role of heat treatment, wherein the zT of $Ti_{0.5}V_{0.5}CoSb$ HH alloy improves upon annealing and zT for TiCoSb and VCoSb HH alloys deteriorates upon annealing. The synthesized biphasic-quaternary $Ti_{0.5}V_{0.5}CoSb$ HH alloy exhibited a $zT_{max} \approx 0.4$ (± 0.05) at 873 K, comparable to as-sintered VCoSb HH alloy, which is driven by its inherently low κ_L. The annealed $Ti_{1-x}V_xCoSb$ ($0.25 < x < 0.75$) exhibits lower κ_L due to the spinodal decomposition, unlike TiCoSb and VCoSb HH alloys, as shown in Figure 4f. The measured κ_L is the lowest when compared with the previously reported VEC ~ 18 HH alloys ZrCoSb,[58] VFeSb,[17] NbFeSb,[68] TaFeSb,[69] ZrNiSn,[41] NbCoSn,[70] and TaCoSn.[70] A further enhancement in the power factor of the biphasic-quaternary $Ti_{0.5}V_{0.5}CoSb$ HH can be achieved via the electronic doping of the Co or Sb crystallographic site, while grain size reduction and panoscopic approaches may provide a further reduction in κ_L.[40−43]

6. CONCLUSIONS

In this work, we report biphasic-quaternary $Ti_{0.5}V_{0.5}CoSb$ HH alloy with nominal VEC ≈ 18.5, exhibiting biphasic microstructure upon annealing and innately reduced κ_L, altogether resulting in prospective n-type TE material for high-temperature thermoelectric applications. A significant alteration in the TE transport properties was achieved by the heat treatment of the HH alloys synthesized employing arc melting and spark plasma sintering. Remarkably, the occurrence of spinodal decomposition and alloy scattering supplemented by mass and strain fluctuation in biphasic-quaternary $Ti_{0.5}V_{0.5}CoSb$ HH alloy was reflected in its reduced lattice thermal conductivity of ≈2 W m^{-1} K^{-1} in a wide temperature range (300−873 K), thus achieving a maximum $zT \approx 0.4$ (± 0.05) at 873 K. For annealed and thermally stable HH alloys, the evaluated zT value for $Ti_{0.5}V_{0.5}CoSb$ corresponds to significant enhancement over pristine ternary TiCoSb (≈4 times) and VCoSb (≈2 times) HH phases. The synthesized biphasic-quaternary HH alloy was found to be thermally stable up to ≈1000 K, and its zT might be further enhanced using the future tuning of the chemical composition, nanostructuring, and panoscopic approaches.[40,43] The experimental outcomes of the thermoelectric transport property measurements were corroborated by theoretical calculations, which display favorable modification in the electronic DOS and phonon dispersion for biphasic-quaternary $Ti_{0.5}V_{0.5}CoSb$ HH alloy. This study provides fundamental insights into the discovery of novel biphasic-quaternary HH derivative alloys with intrinsically low κ_L and highlights the critical role of heat treatment of HH alloys for prospective thermoelectric applications.

■ ASSOCIATED CONTENT

Data Availability Statement

The data that support the findings of this study are available upon request from the authors.

Supporting Information

The Supporting Information is available free of charge at https://pubs.acs.org/doi/10.1021/acsami.2c16595.

Thermal stability of transport properties over a thermal cycle of biphasic-quaternary $Ti_{0.5}V_{0.5}CoSb$ half-Heusler alloy; disorder parameter calculations for nominal $Ti_{1-x}V_xCoSb$ ($0 < x < 1$) alloys; Rietveld refinement XRD patterns; and spin-polarized band structure and density of states of VCoSb and $Ti_{0.5}V_{0.5}CoSb$ half-Heusler alloy (PDF)

■ AUTHOR INFORMATION

Corresponding Authors

Nagendra S. Chauhan − *Department of Applied Physics, Graduate School of Engineering, Tohoku University, Sendai 980-8579 Miyagi, Japan; Nanochemistry Research Group, International Iberian Nanotechnology Laboratory (INL), Braga 4715-330, Portugal; Department of Material Science & Engineering, Indian Institute of Technology, Kanpur 208016 Uttar Pradesh, India;* orcid.org/0000-0003-2579-6642; Email: nagendra599@gmail.com

https://doi.org/10.1021/acsami.2c16595
ACS Appl. Mater. Interfaces 2022, 14, 54736−54747

Amrita Bhattacharya − *Department of Metallurgical Engineering & Material Science, Indian Institute of Technology, Mumbai 400076 Maharashtra, India;* orcid.org/0000-0002-7389-7387; Email: b_amrita@iitb.ac.in

Authors

Dipanwita Bhattacharjee − *Department of Metallurgical Engineering & Material Science, Indian Institute of Technology, Mumbai 400076 Maharashtra, India*

Tanmoy Maiti − *Department of Material Science & Engineering, Indian Institute of Technology, Kanpur 208016 Uttar Pradesh, India;* orcid.org/0000-0003-1581-7614

Yury V. Kolen'ko − *Nanochemistry Research Group, International Iberian Nanotechnology Laboratory (INL), Braga 4715-330, Portugal;* orcid.org/0000-0001-7493-1762

Yuzuru Miyazaki − *Department of Applied Physics, Graduate School of Engineering, Tohoku University, Sendai 980-8579 Miyagi, Japan;* orcid.org/0000-0002-3178-5838

Complete contact information is available at: https://pubs.acs.org/10.1021/acsami.2c16595

Author Contributions

⊥N.S.C. and D.B. contributed equally.

Notes

The authors declare no competing financial interest.

■ ACKNOWLEDGMENTS

This work was supported by Science Education and Research Board (SERB) under the IMPRINT project (SPO/SERB/MET/2018547), the DST Inspire faculty project (DST/INSPIRE/04/2015/000089), the IITB seed grant project (RD/0517-IRCCSH0-043), and SERB ECRA project (ECR/2018/002356). The high-performance computational facilities (viz., Aron (Ab-CMS Lab, IITB), Dendrite (ME&MS Department, IITB), and Spacetime, IITB) and CDAC Pune (Param Yuva-II) are acknowledged for providing computational hours. Y.V.K. thanks the Portuguese Foundation for Science and Technology (FCT) for support under the CritMag Project (PTDC/NAN-MAT/28745/2017).

■ REFERENCES

(1) Offernes, L.; Ravindran, P.; Kjekshus, A. Electronic Structure and Chemical Bonding in Half-Heusler Phases. *J. Alloys Compd.* **2007**, *439*, 37−54.

(2) Casper, F.; Graf, T.; Chadov, S.; Balke, B.; Felser, C. Half-Heusler Compounds: Novel Materials for Energy and Spintronic Applications. *Semicond. Sci. Technol.* **2012**, *27*, No. 063001.

(3) Lin, H.; Wray, L. A.; Xia, Y.; Xu, S.; Jia, S.; Cava, R. J.; Bansil, A.; Hasan, M. Z. Half-Heusler Ternary Compounds as New Multifunctional Experimental Platforms for Topological Quantum Phenomena. *Nat. Mater.* **2010**, *9*, 546−549.

(4) Quinn, R. J.; Bos, J.-W. G. Advances in Half-Heusler Alloys for Thermoelectric Power Generation. *Mater. Adv.* **2021**, *2*, 6246−6266.

(5) Zeier, W. G.; Schmitt, J.; Hautier, G.; Aydemir, U.; Gibbs, Z. M.; Felser, C.; Snyder, G. J. Engineering Half-Heusler Thermoelectric Materials Using Zintl Chemistry. *Nat. Rev. Mater.* **2016**, *1*, No. 16032.

(6) Chen, S.; Ren, Z. Recent Progress of Half-Heusler for Moderate Temperature Thermoelectric Applications. *Mater. Today* **2013**, *16*, 387−395.

(7) Anand, S.; Xia, K.; Hegde, V. I.; Aydemir, U.; Kocevski, V.; Zhu, T.; Wolverton, C.; Snyder, G. J. A Valence Balanced Rule for Discovery of 18-Electron Half-Heuslers with Defects. *Energy Environ. Sci.* **2018**, *11*, 1480−1488.

(8) Dylla, M. T.; Dunn, A.; Anand, S.; Jain, A.; Snyder, G. J. Machine Learning Chemical Guidelines for Engineering Electronic Structures in Half-Heusler Thermoelectric Materials. *Research* **2020**, *2020*, No. 6375171.

(9) Raghuvanshi, P. R.; Mondal, S.; Bhattacharya, A. A High Throughput Search for Efficient Thermoelectric Half-Heusler Compounds. *J. Mater. Chem. A* **2020**, *8*, 25187−25197.

(10) Graf, T.; Parkin, S. S. P.; Felser, C. Heusler Compounds - A Material Class with Exceptional Properties. *IEEE Trans. Magn.* **2011**, *47*, 367−373.

(11) Kandpal, H. C.; Felser, C.; Seshadri, R. Covalent Bonding and the Nature of Band Gaps in Some Half-Heusler Compounds. *J. Phys. D: Appl. Phys.* **2006**, *39*, No. 776.

(12) Toberer, E. S.; Zevalkink, A.; Snyder, G. J. Phonon Engineering through Crystal Chemistry. *J. Mater. Chem.* **2011**, *21*, 15843−15852.

(13) Chauhan, N. S.; Bathula, S.; Vishwakarma, A.; Bhardwaj, R.; Johari, K. K.; Gahtori, B.; Dhar, A. Enhanced Thermoelectric Performance in P-Type ZrCoSb Based Half-Heusler Alloys Employing Nanostructuring and Compositional Modulation. *J. Materiomics* **2019**, *5*, 94−102.

(14) Chauhan, N. S.; Bathula, S.; Vishwakarma, A.; Bhardwaj, R.; Johari, K. K.; Gahtori, B.; Saravanan, M.; Dhar, A. Compositional Tuning of ZrNiSn Half-Heusler Alloys: Thermoelectric Characteristics and Performance Analysis. *J. Phys. Chem. Solids* **2018**, *123*, 105−112.

(15) Chauhan, N. S.; Miyazaki, Y. Low Lattice Thermal Conductivity and Microstructural Evolution in VFeSb Half-Heusler Alloys. *Materialia* **2022**, *22*, No. 101430.

(16) Kocevski, V.; Wolverton, C. Designing High-Efficiency Nanostructured Two-Phase Heusler Thermoelectrics. *Chem. Mater.* **2017**, *29*, 9386−9398.

(17) Chauhan, N. S.; Miyazaki, Y. Low Lattice Thermal Conductivity and Microstructural Evolution in VFeSb Half-Heusler Alloys. *Materialia* **2022**, *22*, No. 101430.

(18) Chauhan, N. S.; Raghuvanshi, P. R.; Tyagi, K.; Johari, K. K.; Tyagi, L.; Gahtori, B.; Bathula, S.; Bhattacharya, A.; Mahanti, S. D.; Singh, V. N.; Kolen'ko, Yv.; Dhar, A. Defect Engineering for Enhancement of Thermoelectric Performance of (Zr,Hf)NiSn-Based n-Type Half-Heusler Alloys. *J. Phys. Chem. C* **2020**, *124*, 8584−8593.

(19) Xia, K.; Nan, P.; Tan, S.; Wang, Y.; Ge, B.; Zhang, W.; Anand, S.; Zhao, X.; Snyder, G. J.; Zhu, T. Short-Range Order in Defective Half-Heusler Thermoelectric Crystals. *Energy Environ. Sci.* **2019**, *12*, 1568−1574.

(20) Anand, S.; Xia, K.; Hegde, V. I.; Aydemir, U.; Kocevski, V.; Zhu, T.; Wolverton, C.; Snyder, G. J. A Valence Balanced Rule for Discovery of 18-Electron Half-Heuslers with Defects. *Energy Environ. Sci.* **2018**, *11*, 1480−1488.

(21) Chauhan, N. S.; Gahtori, B.; Sivaiah, B.; Mahanti, S. D.; Dhar, A.; Bhattacharya, A. Modulating the Lattice Dynamics of N-Type Heusler Compounds via Tuning Ni Concentration. *Appl. Phys. Lett.* **2018**, *113*, No. 013902.

(22) Misra, D. K.; Rajput, A.; Bhardwaj, A.; Chauhan, N. S.; Singh, S. Enhanced Power Factor and Reduced Thermal Conductivity of a Half-Heusler Derivative Ti9Ni7Sn8: A Bulk Nanocomposite Thermoelectric Material. *Appl. Phys. Lett.* **2015**, *106*, No. 103901.

(23) Chauhan, N. S.; Bathula, S.; Vishwakarma, A.; Bhardwaj, R.; Gahtori, B.; Srivastava, A. K.; Saravanan, M.; Dhar, A. A Nanocomposite Approach for Enhancement of Thermoelectric Performance in Hafnium-Free Half-Heuslers. *Materialia* **2018**, *1*, 168−174.

(24) Poon, S. J.; Wu, D.; Zhu, S.; Xie, W.; Tritt, T. M.; Thomas, P.; Venkatasubramanian, R. Half-Heusler Phases and Nanocomposites as Emerging High-ZT Thermoelectric Materials. *J. Mater. Res.* **2011**, *26*, 2795−2802.

(25) Miranda, J.; Gruhn, T. Interplay Between Electronic States and Structural Stability in Cation-Deficient VCoSb, NbCoSb, and TaCoSb Half-Heuslers. *J. Electron. Mater.* **2022**, *51*, 2043−2053.

(26) Li, S.; Bai, F.; Wang, R.; Chen, C.; Li, X.; Cao, F.; Yu, B.; Sui, J.; Liu, X.; Ren, Z.; Zhang, Q. Titanium Doping to Enhance Thermoelectric Performance of 19-Electron VCoSb Half-Heusler Compounds with Vanadium Vacancies. *Ann. Phys.* **2020**, *532*, No. 1900440.
(27) Zhang, H.; Wang, Y.; Huang, L.; Chen, S.; Dahal, H.; Wang, D.; Ren, Z. Synthesis and Thermoelectric Properties of N-Type Half-Heusler Compound VCoSb with Valence Electron Count of 19. *J. Alloys Compd.* **2016**, *654*, 321−326.
(28) Huang, L.; Wang, J.; Mo, X.; Lei, X.; Ma, S.; Wang, C.; Zhang, Q. Improving the Thermoelectric Properties of the Half-Heusler Compound VCoSb by Vanadium Vacancy. *Materials* **2019**, *12*, No. 1637.
(29) Ferluccio, D. A.; Halpin, J. E.; Macintosh, K. L.; Quinn, R. J.; Don, E.; Smith, R. I.; Maclaren, D. A.; Bos, J. W. G. Low Thermal Conductivity and Promising Thermoelectric Performance in A: XCoSb (A = V, Nb or Ta) Half-Heuslers with Inherent Vacancies. *J. Mater. Chem. C* **2019**, *7*, 6539−6547.
(30) Ferluccio, D. A.; Smith, R. I.; Buckman, J.; Bos, J. W. G. Impact of Nb Vacancies and P-Type Doping of the NbCoSn-NbCoSb Half-Heusler Thermoelectrics. *Phys. Chem. Chem. Phys.* **2018**, *20*, 3979−3987.
(31) Huang, L.; He, R.; Chen, S.; Zhang, H.; Dahal, K.; Zhou, H.; Wang, H.; Zhang, Q.; Ren, Z. A New N-Type Half-Heusler Thermoelectric Material NbCoSb. *Mater. Res. Bull.* **2015**, *70*, 773−778.
(32) Wollmann, L.; Nayak, A. K.; Parkin, S. S. P.; Felser, C. Heusler 4.0: Tunable Materials. *Annu. Rev. Mater. Res.* **2017**, *47*, 247−270.
(33) Anand, S.; Wood, M.; Xia, Y.; Wolverton, C.; Snyder, G. J. Double Half-Heuslers. *Joule* **2019**, *3*, 1226−1238.
(34) Fecher, G. H.; Rausch, E.; Balke, B.; Weidenkaff, A.; Felser, C. Half-Heusler Materials as Model Systems for Phase-Separated Thermoelectrics. *Phys. Status Solidi (A)* **2016**, *213*, 716−731.
(35) Schwall, M.; Balke, B. On the Phase Separation in N-Type Thermoelectric Half-Heusler Materials. *Materials* **2018**, *11*, No. 649.
(36) Page, A.; van der Ven, A.; Poudeu, P. F. P.; Uher, C. Origins of Phase Separation in Thermoelectric (Ti, Zr, Hf)NiSn Half-Heusler Alloys from First Principles. *J. Mater. Chem. A* **2016**, *4*, 13949−13956.
(37) Berche, A.; Tédenac, J. C.; Jund, P. Phase Separation in the Half-Heusler Thermoelectric Materials (Hf,Ti,Zr)NiSn. *Scr. Mater.* **2017**, *139*, 122−125.
(38) Rausch, E.; Balke, B.; Stahlhofen, J. M. J. M.; Ouardi, S.; Burkhardt, U.; Felser, C. Fine Tuning of Thermoelectric Performance in Phase-Separated Half-Heusler Compounds. *J. Mater. Chem. C* **2015**, *3*, 10409−10414.
(39) Johari, K. K.; Sharma, D. K.; Verma, A. K.; Bhardwaj, R.; Chauhan, N. S.; Kumar, S.; Singh, M. N.; Bathula, S.; Gahtori, B. In Situ Evolution of Secondary Metallic Phases in Off-Stoichiometric ZrNiSn for Enhanced Thermoelectric Performance. *ACS Appl. Mater. Interfaces* **2022**, *14*, 19579−19593.
(40) Zhao, L. D.; Dravid, V. P.; Kanatzidis, M. G. The Panoscopic Approach to High Performance Thermoelectrics. *Energy Environ. Sci.* **2014**, *7*, 251−268.
(41) Chauhan, N. S.; Bathula, S.; Vishwakarma, A.; Bhardwaj, R.; Gahtori, B.; Kumar, A.; Dhar, A. Vanadium-Doping-Induced Resonant Energy Levels for the Enhancement of Thermoelectric Performance in Hf-Free ZrNiSn Half-Heusler Alloys. *ACS Appl. Energy Mater.* **2018**, *1*, 757−764.
(42) Chauhan, N. S.; Bhardwaj, A.; Senguttuvan, T. D.; Pant, R. P.; Mallik, R. C.; Misra, D. K. A Synergistic Combination of Atomic Scale Structural Engineering and Panoscopic Approach in P-Type ZrCoSb-Based Half-Heusler Thermoelectric Materials for Achieving High ZT. *J. Mater. Chem. C* **2016**, *4*, 5766−5778.
(43) He, J.; Kanatzidis, M. G.; Dravid, V. P. High Performance Bulk Thermoelectrics via a Panoscopic Approach. *Mater. Today* **2013**, *16*, 166−176.
(44) Degen, T.; Sadki, M.; Bron, E.; Konig, U.; Nenert, G. The highscore suite. *Powder Diffr* **2014**, *29* (S2), S13−S18.
(45) Rodríguez-Carvajal, J. Recent advances in magnetic structure determination by neutron powder diffraction. *Phys. B Condens. Matter* **1993**, *192* (1−2), 55−69.
(46) Rodríguez-Carvajal, J.Recent Developments of the Program FULLPROF. *Commission on powder diffraction (IUCr). Newsletter*2001, *26*, 12−19.
(47) Kohn, W.; Sham, L. J. Self-Consistent Equations Including Exchange and Correlation Effects. *Phys. Rev.* **1965**, *140*, No. A1133.
(48) Kresse, G.; Hafner, J. Ab Initio Molecular-Dynamics Simulation of the Liquid-Metal−Amorphous-Semiconductor Transition in Germanium. *Phys. Rev. B* **1994**, *49*, No. 14251.
(49) Kresse, G.; Hafner, J. Ab Initio Molecular-Dynamics Simulation of the Liquid-Metal−Amorphous-Semiconductor Transition in Germanium. *Phys. Rev. B* **1994**, *49*, No. 14251.
(50) Hafner, J.; Kresse, G.The Vienna Ab-Initio Simulation Program VASP: An Efficient and Versatile Tool for Studying the Structural, Dynamic, and Electronic Properties of Materials. In *Properties of Complex Inorganic Solids*; Springer, 1997; pp 69−82.
(51) Perdew, J. P.; Burke, K.; Ernzerhof, M. Generalized Gradient Approximation Made Simple. *Phys. Rev. Lett.* **1996**, *77*, No. 3865.
(52) Monkhorst, H. J.; Pack, J. D. Special Points for Brillouin-Zone Integrations. *Phys. Rev. B* **1976**, *13*, No. 5188.
(53) Togo, A.; Tanaka, I. First Principles Phonon Calculations in Materials Science. *Scr. Mater.* **2015**, *108*, 1−5.
(54) Madsen, G. K. H.; Carrete, J.; Verstraete, M. J. BoltzTraP2, a Program for Interpolating Band Structures and Calculating Semi-Classical Transport Coefficients. *Comput. Phys. Commun.* **2018**, *231*, 140−145.
(55) Zou, D. F.; Xie, S. H.; Liu, Y. Y.; Lin, J. G.; Li, J. Y. Electronic Structure and Thermoelectric Properties of Half-Heusler Zr0. 5Hf0. 5NiSn by First-Principles Calculations. *J. Appl. Phys.* **2013**, *113*, No. 193705.
(56) Sekimoto, T.; Kurosaki, K.; Muta, H.; Yamanaka, S. Annealing Effect on Thermoelectric Properties of TiCoSb Half-Heusler Compound. *J. Alloys Compd.* **2005**, *394*, 122−125.
(57) Vishwakarma, A.; Chauhan, N. S.; Bhardwaj, R.; Johari, K. K.; Dhakate, S. R.; Gahtori, B.; Bathula, S. Compositional Modulation Is Driven by Aliovalent Doping in N-Type TiCoSb Based Half-Heuslers for Tuning Thermoelectric Transport. *Intermetallics* **2020**, *125*, No. 106914.
(58) Chauhan, N. S.; Bathula, S.; Gahtori, B.; Kolen'ko, Y. V.; Dhar, A. Enhanced Thermoelectric Performance in Hf-Free p-Type (Ti, Zr)CoSb Half-Heusler Alloys. *J. Electron. Mater.* **2019**, *48*, 6700−6709.
(59) Johari, K. K.; Bhardwaj, R.; Chauhan, N. S.; Bathula, S.; Auluck, S.; Dhakate, S. R.; Gahtori, B. High Thermoelectric Performance in N-Type Degenerate ZrNiSn-Based Half-Heusler Alloys Driven by Enhanced Weighted Mobility and Lattice Anharmonicity. *ACS Appl. Energy Mater.* **2021**, *4*, 3393−3403.
(60) Johari, K. K.; Bhardwaj, R.; Chauhan, N. S.; Gahtori, B.; Bathula, S.; Auluck, S.; Dhakate, S. R. Band Structure Modification and Mass Fluctuation Effects of Isoelectronic Germanium-Doping on Thermoelectric Properties of ZrNiSn. *ACS Appl. Energy Mater.* **2020**, *3*, 1349−1357.
(61) Kim, H.-S. S.; Gibbs, Z. M.; Tang, Y.; Wang, H.; Snyder, G. J. Characterization of Lorenz Number with Seebeck Coefficient Measurement. *APL Mater.* **2015**, *3*, No. 041506.
(62) Wang, L. L.; Miao, L.; Wang, Z. Y.; Wei, W.; Xiong, R.; Liu, H. J.; Shi, J.; Tang, X. F. Thermoelectric Performance of Half-Heusler Compounds TiNiSn and TiCoSb. *J. Appl. Phys.* **2009**, *105*, No. 013709.
(63) Tobola, J.; Pierre, J.; Kaprzyk, S.; Skolozdra, R. V.; Kouacou, M. A. Crossover from Semiconductor to Magnetic Metal in Semi-Heusler Phases as a Function of Valence Electron Concentration. *J. Phys. Condens. Matter* **1998**, *10*, 1013−1032.
(64) Tian, Z.; Esfarjani, K.; Shiomi, J.; Henry, A. S.; Chen, G. On the Importance of Optical Phonons to Thermal Conductivity in Nanostructures. *Appl. Phys. Lett.* **2011**, *99*, No. 053122.

https://doi.org/10.1021/acsami.2c16595
ACS Appl. Mater. Interfaces 2022, 14, 54736−54747

(65) Raghuvanshi, P. R.; Bhattacharjee, D.; Bhattacharya, A. Self-Doping for Synergistically Tuning the Electronic and Thermal Transport Coefficients in n-Type Half-Heuslers. *ACS Appl. Mater. Interfaces* **2021**, *13*, 55060−55071.
(66) Zhang, Y. First-Principles Debye−Callaway Approach to Lattice Thermal Conductivity. *J. Materiomics* **2016**, *2*, 237−247.
(67) Raghuvanshi, P. R.; Mondal, S.; Bhattacharya, A. A High Throughput Search for Efficient Thermoelectric Half-Heusler Compounds. *J. Mater. Chem. A* **2020**, *8*, 25187−25197.
(68) Silpawilawan, W.; Kurosaki, K.; Ohishi, Y.; Muta, H.; Yamanaka, S. FeNbSb P-Type Half-Heusler Compound: Beneficial Thermomechanical Properties and High-Temperature Stability for Thermoelectrics. *J. Mater. Chem. C* **2017**, *5*, 6677−6681.
(69) Zhu, H.; Mao, J.; Li, Y.; Sun, J.; Wang, Y.; Zhu, Q.; Li, G.; Song, Q.; Zhou, J.; Fu, Y.; He, R.; Tong, T.; Liu, Z.; Ren, W.; You, L.; Wang, Z.; Luo, J.; Sotnikov, A.; Bao, J.; Nielsch, K.; Chen, G.; Singh, D. J.; Ren, Z. Discovery of TaFeSb-Based Half-Heuslers with High Thermoelectric Performance. *Nat. Commun.* **2019**, *10*, No. 270.
(70) Li, S.; Zhu, H.; Mao, J.; Feng, Z.; Li, X.; Chen, C.; Cao, F.; Liu, X.; Singh, D. J.; Ren, Z.; Zhang, Q. N-Type TaCoSn-Based Half-Heuslers as Promising Thermoelectric Materials. *ACS Appl. Mater. Interfaces* **2019**, *11*, 41321−41329.

NOTE ADDED AFTER ASAP PUBLICATION

This paper originally published ASAP on November 30, 2022. An error in the 4th column of Table 2 was corrected, and a new version was reposted on December 14, 2022.

https://doi.org/10.1021/acsami.2c16595
ACS Appl. Mater. Interfaces 2022, 14, 54736−54747